



**US Army Corps
of Engineers®**
Engineer Research and
Development Center

ERDC
INNOVATIVE SOLUTIONS
for a safer, better world

ERDC 6.1 Basic Research

Measuring the Non-Line-of-Sight Ultra-High-Frequency Channel in Mountainous Terrain

A Spread-Spectrum, Portable Channel Sounder

Samuel S. Streeter, Daniel J. Breton,
and Johnathan M. Corgan

March 2018



The U.S. Army Engineer Research and Development Center (ERDC) solves the nation's toughest engineering and environmental challenges. ERDC develops innovative solutions in civil and military engineering, geospatial sciences, water resources, and environmental sciences for the Army, the Department of Defense, civilian agencies, and our nation's public good. Find out more at www.erdclibrary.usace.army.mil.

To search for other technical reports published by ERDC, visit the ERDC online library at <http://acwc.sdp.sirsi.net/client/default>.

Measuring the Non-Line-of-Sight Ultra-High-Frequency Channel in Mountainous Terrain

A Spread-Spectrum, Portable Channel Sounder

Samuel S. Streeter and Daniel J. Breton

*U.S. Army Engineer Research and Development Center (ERDC)
Cold Regions Research and Engineering Laboratory (CRREL)
72 Lyme Road
Hanover, NH 03755*

Johnathan M. Corgan

*Corgan Labs
6081 Meridian Avenue
San Jose, CA 95120*

Final Report

Approved for public release; distribution is unlimited.

Prepared for U.S. Army Corps of Engineers
Washington, DC 20314-1000

Under ERDC 6.1 Basic Research
Project 462178, "Wide-Band Radio Frequency Propagation"

Abstract

Very few measurements campaigns have conducted ground-based, radio-frequency propagation field measurement campaigns conducted in deep mountainous terrain, and none have focused on the non-line-of-sight channel in mountain shadow zones. Here, we introduce a versatile, spread-spectrum, portable channel sounder specifically designed to measure the non-line-of-sight, ultra-high-frequency channel in mountainous terrain. The receiver is backpack mounted for ease of transport into remote, mountainous locations that are kilometers from the transmitter and inaccessible to vehicles of any kind. The system uses software-defined radios to transmit and capture a wideband pseudorandom noise waveform and maintains synchronization using reference signals from rubidium clocks trained by global positioning system signals. A clock holdover capability maintains system synchronization within tens of nanoseconds even when global positioning system signals are unavailable. System synchronization allows for coherent captures up to 60 seconds in duration and provides a dynamic range of more than 30 decibels. The system exhibits a timing uncertainty of ± 145 nanoseconds, corresponding to ± 44 meters. Measured channel power–delay profiles are verified using geospatial analyses. Initial results suggest that local topography strongly affects channel time dispersion characteristics and that a given set of channel conditions cannot be readily generalized to cover an entire mountainous region.

DISCLAIMER: The contents of this report are not to be used for advertising, publication, or promotional purposes. Citation of trade names does not constitute an official endorsement or approval of the use of such commercial products. All product names and trademarks cited are the property of their respective owners. The findings of this report are not to be construed as an official Department of the Army position unless so designated by other authorized documents.

DESTROY THIS REPORT WHEN NO LONGER NEEDED. DO NOT RETURN IT TO THE ORIGINATOR.

Contents

Abstract	ii
Figures	iv
Preface	v
Acronyms and Abbreviations	vi
1 Introduction	1
1.1 Background	1
1.2 Objectives	2
1.3 Approach	2
2 Channel Measurement Methods	3
2.1 Channel sounding	3
2.2 Multipath channel model	3
2.3 Channel impulse response approximation	4
2.4 Channel sounding for the power–delay profile	6
2.5 System hardware	6
2.6 Channel sounding waveform	9
2.7 System resolution and uncertainty	10
2.8 Postprocessing	11
2.9 Frequency-selective fading	12
2.10 Channel statistics	13
2.11 Geospatial analysis	15
3 Channel Measurement Results	17
3.1 Franconia Notch study area	18
3.2 Great Gulf Wilderness study area	20
3.3 Lyme study area	21
3.3.1 <i>Ranger Trail</i>	21
3.3.1 <i>Acorn Hill</i>	21
3.4 Channel statistics	23
4 Discussion	25
5 Conclusion	26
6 Future Work	27
References	28
Report Documentation Page	

Figures

Figures

- 1 The 23 kg station backpack: (a) from top to bottom, Getac B300 field laptop; external Rb clock; mWISP unit; two solid-state, 24 VDC, 10 A-h LiFePO₄ batteries; and GPS antenna on the right and (b) the station backpack shouldered for transport 8
- 2 The state of New Hampshire and the three-channel sounding study areas..... 17
- 3 Sounding results (5 s capture time for each profile) coupled with geospatial analysis. Covisible regions are highlighted in *red*, and *concentric blue rings* show bistatic path delay time on the maps: (a) power–delay profile from Franconia Notch, (b) map of the Franconia Notch area, (c) power–delay profile from the Great Gulf Wilderness, and (d) map of the Great Gulf Wilderness area..... 19
- 4 Sounding results (5 s capture time for each profile) coupled with geospatial analysis. Covisible regions are highlighted in *red*, and *concentric blue rings* show bistatic path delay time on the GIS maps: (a) power–delay profile from Ranger Trail in Lyme, (b) map of the Ranger Trail area, (c) power–delay profile from Acorn Hill in Lyme, and (d) map of the Acorn Hill area 22
- 5 RMS delay spread data presented as a function of 3-D Tx–Rx separation distance for the three main study areas. A total of 79 profile RMS delay spreads are reported 23

Preface

This study was conducted for the U.S. Army Corps of Engineers, using Military Direct Funds, under Engineer Research and Development Center (ERDC) 6.1 Basic Research Project 462178, “Wide-Band Radio Frequency Propagation.” The technical monitor was Dr. Marino A. Niccolai, ERDC Cold Regions Research and Engineering Laboratory (CRREL).

The work was performed by the Signature Physics Branch (CEERD-RRD) of the Research and Engineering Division (CEERD-RR), ERDC-CRREL. At the time of publication, Dr. Marino A. Niccolai was Chief, CEERD-RRD; Mr. J. D. Horne was Chief, CEERD-RR; and Dr. Mark L. Moran, CEERD-RZT, was the ERDC-CRREL Technical Director for the Military Engineering business area. The Deputy Director of ERDC-CRREL was Dr. Lance D. Hansen, and the ERDC-CRREL Director was Dr. Joseph L. Corriveau.

The authors thank John Carlson at Echo Ridge, LLC, for guidance throughout this project and to the many CRREL personnel who helped collect experimental channel sounding data for this project. All dealt with extremely long field days, heavy loads, and poor communications with tireless enthusiasm and technical expertise.

COL Bryan S. Green was the Commander of ERDC, and Dr. David W. Pittman was the Director.

Acronyms and Abbreviations

3-D	Three-Dimensional
BPSK	Binary Phase-Shift Keying
CIR	Channel Impulse Response
CRREL	Cold Regions Research and Engineering Laboratory
DEM	Digital Elevation Model
GIS	Geographic Information System
GPS	Global Positioning System
GPSDO	GPS-Disciplined Oscillator
GRASS	Geographic Resources Analysis Support System
GUI	Graphical User Interface
IQ	In-Phase and Quadrature
LiFePO ₄	Lithium Iron Phosphate
LOS	Line-Of-Sight
mWISP	Mini Wireless Instrumented Streaming Platform
NLOS	Non-Line-Of-Sight
PN	Pseudorandom Noise
PPS	Pulse Per Second
Rb	Rubidium
RF	Radio Frequency
RMS	Root Mean Squared
Rx	Receiver
SDR	Software-Defined Radio
SNR	Signal-to-Noise Ratio
Tx	Transmitter
UHF	Ultra-High-Frequency
USRP	Universal Software Radio Peripheral
WSSUS	Wide-Sense Stationary Uncorrelated Scattering
λ	Wavelength

1 Introduction

1.1 Background

The non-line-of-sight (NLOS) radio-frequency (RF) channel for ground communications in mountainous terrain exhibits multipath and delayed behavior, causing intersymbol interference and equalization issues at the receiving station (Chuang 1987; Breton and Arcone 2015). Bistatic travel time between a transmitter (Tx) and receiver (Rx) is oftentimes tens of microseconds (de Weck et al. 1988; Driessen 1990, 1991, 1992, 2000; Raekken et al. 1991; Mohr 1993; Sousa et al. 1994) and can even exceed 100 μ s in mountainous terrain (Driessen 1990; Raekken et al. 1991). Typical forms of infrastructure, such as repeaters or cell towers, may not provide complete coverage, if such infrastructure exists at all, a common scenario encountered in areas of military conflict or in the backcountry.

A variety of materials and land coverage types exist in mountainous terrain; and topographic features vary from smooth, forested slopes to scree and boulder fields, wet drainages to exposed bedrock summits. Surface roughness may be on the order of the signal wavelength (λ) or greater, resulting in diffuse scattering (Driessen 1990; Lu et al. 2013). The influence of these heterogeneous, rough surfaces on RF propagation, specifically topographic reflection, is not rigorously understood. Lambertian scattering and channel reciprocity are assumed valid (Lu et al. 2013; Lu and Bertoni 2013); but the literature lacks experimental data to support these assumptions, particularly in NLOS channels in the mountains. These considerations make mountainous terrain a complex problem for RF propagation and communication planning tools. Furthermore, mountainous locations pose significant challenges for experimental research given a general lack of road access, exposure to the elements, difficulties transporting measurement hardware, and so on.

The literature focuses on the characterization of the RF channel near mountainous terrain (Zogg 1987; de Weck et al. 1988; Driessen 1990, 1991, 1992, 2000; Maeyama et al. 1993; Mohr 1993; Lu et al. 2013; Lu and Bertoni 2013). These efforts emphasize channel statistics between communicating stations that are line-of-sight (LOS) or NLOS on relatively flat

ground with mountains nearby, not the channel between stations located deep within mountainous terrain, especially those at different elevations.

1.2 Objectives

The objectives of this project are (1) to create a method of experimentally quantifying the time dispersion and multipath characteristics of the ground-to-ground NLOS ultra-high-frequency (UHF) channel in mountainous terrain and (2) to generate an experimental basis for guiding the creation of a deterministic approach to predicting channel behavior for ground communications in the mountains.

1.3 Approach

To accomplish these objectives, we developed a spread-spectrum, foot-portable, software-defined, radio-based channel sounding system that is the first of its kind. The sounding system measures channel power–delay profiles in deep mountainous terrain, which provide valuable channel time dispersion and multipath information. In this report, we present bistatic channel measurements from three remote, mountainous areas in New Hampshire. We use geospatial analyses to validate system operation and to examine the influence of local topographic features on individual power–delay-profile curves. Through this work, we contribute to a deterministic approach to understanding the channel in mountainous terrain given equipment parameters and terrain information.

2 Channel Measurement Methods

2.1 Channel sounding

Channel sounding is an experimental technique used to measure the transfer function of a propagation environment. In the RF field, this transfer function is otherwise known as the RF channel. The technique involves the transmission and capture of a known test signal between sounding stations, commonly followed by cross-correlation of the received signal with the original signal (Papazian and Lemmon 2011). We developed a channel sounding system specifically for measuring the bistatic, NLOS, UHF channel in mountainous terrain. The channel sounding system uses a wideband sounding signal. The term “wideband” implies that the signal is wider in bandwidth than that used by typical radio systems (Newhall et al. 1996), so the system is capable of capturing signal delay and multipathing effects throughout a study area.

2.2 Multipath channel model

The RF channel can be thought of as a time-domain transfer function, $h[t]$, which is commonly referred to as the channel impulse response (CIR). The CIR model for a bistatic multipath channel is (Rappaport 2002; Salous 2013)

$$h[t] = \sum_{i=1}^L \alpha_i e^{j\varphi_i} \delta(t - \tau_i). \quad (1)$$

Here, L is the total number of multipath components in the channel, and α_i , φ_i , and τ_i are the amplitude, phase, and delay of the i th multipath component, respectively. Multipath components arrive at the Rx at different delay times with a range of amplitudes and phases. The phase, φ_i , depends on the component path length and changes by 2π when the path length changes by a wavelength. Multipath component amplitudes assume a range of statistical behaviors between a Rayleigh distribution, when no single dominant propagation path exists in the channel, and a Rician distribution, when a dominant and relatively high-power multipath component exists in the channel (Gans 1972; Sklar 1997). A channel with Rayleigh-distributed signal amplitude will exhibit uniformly distributed phase

over $[0, 2\pi)$ (Doukas and Kalivas 2006). A channel with Rician-distributed signal amplitude will have a phase distribution that is nonuniform over $[0, 2\pi)$, biased to the phase of the dominant component. In a complex environment (e.g., in mountainous terrain), one or both component distributions will be relevant depending on the geometry of the communicating stations and the positioning of features and obstacles (e.g., topography).

2.3 Channel impulse response approximation

The CIR, $h[t]$, relates the complex-valued transmitted signal (i.e., input), $x[t]$, and the complex-valued received signal (i.e., output), $y[t]$, via the convolution function (Papazian and Lemmon 2011), which is

$$y[t] = x[t] * h[t] + n[t]. \quad (2)$$

Here, $*$ is the convolution operator, and $n[t]$ is an additive noise term. The explicit, discrete time representation of equation (2) is

$$y[t] = \sum_{\tau=-\infty}^{\infty} h[\tau]x[t - \tau] + n[t]. \quad (3)$$

Here, τ is delay time or the travel time of a signal between two stations. The discrete time representation of cross-correlation between two N -element long, stationary, complex-valued signals, x_1 and x_2 , is approximated by

$$R_{12}[k] = \frac{1}{N+1} \sum_{m=0}^N \bar{x}_1[m]x_2[m+k]. \quad (4)$$

Here, \bar{x}_1 denotes the complex conjugate of x_1 , and the parameter k is any integer. (If two signals are not of equal length, the shorter signal can be zero padded until it is of equal length to the longer signal.) In the frequency domain, cross-correlation is approximated by the product of the Fourier Transforms of \bar{x}_1 and x_2 ,

$$R_{12} \cong F^{-1}(F(\bar{x}_1)F(x_2)), \quad (5)$$

where $F^{-1}(\cdot)$ is the Inverse Fast Fourier Transform, and $F(\cdot)$ is the Fast Fourier Transform. Importantly, the frequency-domain definition of cross-correlation does not include normalization, which has important implications for the amplitude of the result, R_{12} . For the present study, the cross-correlation result is normalized to the highest value in R_{12} , and results are presented in units of normalized power in decibels. This concept is discussed in more detail in section 2.8.

Using equation (5), correlating each side of equation (3) with a transmitted signal, $x[t]$, yields

$$R_{xy}[\tau] = h[\tau] * R_{xx}[\tau]. \quad (6)$$

Here, R_{xy} is the cross-correlation function of $x[t]$ and $y[t]$, and R_{xx} is the autocorrelation function of $x[t]$. The additive noise component is dropped because $x[t]$ and $n[t]$ are assumed to be uncorrelated (Papazian and Lemon 2011).

A useful channel sounding waveform is a pseudorandom noise (PN) sequence (Cox and Leck 1975; Bultitude 1987; Rappaport 2002; Salous 2013). A PN sequence has beneficial autocorrelation properties. That is, the autocorrelation of a PN sequence is very low at all nonzero shift values. At a shift value of zero, the correlation value is relatively high. The longer the PN sequence, the more the autocorrelation, R_{xx} , resembles a delta function (Rappaport 2002). By the sifting property of the delta function, when R_{xx} resembles a delta function, R_{xy} becomes a good approximation of the CIR, $h[\tau]$. (The dependence of CIR estimation on PN sequence length has been studied, for example, by Novosel and Šišul (2014); but such analysis goes beyond the scope of this paper. Section 2.6 discusses the PN length chosen for the channel sounding system in the present study.) Assuming that R_{xx} is very similar to a delta function, the following adjustment to equation (6) is justified:

$$R_{xy}[\tau] \cong h[\tau] \quad (7)$$

Thus, if R_{xx} resembles a delta function and R_{xy} can be measured, an approximation of the CIR is possible.

The Wide-Sense Stationary Uncorrelated Scattering (WSSUS) channel model assumes that radio channels are stationary over short periods of time and over short spatial distances, fading statistics do not change over short periods of time, the autocorrelation function is independent of absolute time, and power contributions from different multipath components are uncorrelated. The WSSUS model is assumed valid for the bistatic channels investigated in this work so that the measured CIR is considered a representative approximation of the channel (Papazian and Lemmon 2011). Multipath channels that satisfy the WSSUS model fall into two categories: LOS channels exhibiting Rician-distributed signal amplitudes and NLOS channels exhibiting Rayleigh-distributed signal amplitudes. An in-depth explanation of the WSSUS model is given in Salous (2013).

2.4 Channel sounding for the power–delay profile

The power–delay profile is the average squared magnitude of all CIR traces in a continuous channel sounding measurement. A delay profile provides useful channel delay and multipathing information and is defined as (Cox and Leck 1975; Durgin et al. 2003)

$$P[\tau] = 10 \log_{10} \langle |h[\tau]|^2 \rangle. \quad (8)$$

A power–delay profile includes all multipath component power contributions in the channel. The power of each data point in a profile is the sum of all power contributions from equal-length, bistatic components that arrive at the Rx at the same time (i.e., within the same delay bin). Our system experimentally approximates the channel power–delay profile by measuring R_{xy} in equation (7).

2.5 System hardware

The single-input, single-output channel sounding system comprises a dedicated Tx station and a separate, dedicated Rx station, both of which are portable on foot. The backpack-mounted Rx allows for the measurement of bistatic, NLOS channels from in deep mountainous terrain. Each sounding station uses an Echo Ridge LLC Mini Wireless Instrumented Streaming Platform (mWISP), which is software-defined radio (SDR)–based, containing an Ettus Research N200 Universal Software Radio Peripheral

(USRP) and Ettus Research UBX daughterboard. To our knowledge, this is the first foot-portable, SDR-based system of its kind.

The SDR system is versatile with respect to signal frequency and bandwidth parameters and is capable of transmitting arbitrary sounding waveforms. This versatility allows the system to readily measure channels across the UHF spectrum and to switch between different sounding waveforms. Each station mWISP is controlled via Ethernet connection to a Getac B300 field laptop.

The system has the following features: operational frequency range of 20 to 4200 MHz, 25 MHz maximum transmission bandwidth, 20 W maximum transmission power, portable 23 kg Rx backpack unit with battery capacity for over 6 hours of continuous operation, and 500 GB of onboard disk space for storing 1.2 hours of captured data at a maximum Rx sampling rate of 25 MS/s. The Tx design for the 2016 field season was portable on foot in a large waterproof case but had to be collapsed for moving between locations.

Each mWISP USRP uses a one pulse per second (1 PPS) global positioning system (GPS) signal and a 10 MHz frequency signal as timing references. The reference signals are generated by a GPS-disciplined oscillator (GPSDO) in a FEI-Zyfer NanoSync IV rubidium (Rb) clock with each station. Each clock provides a holdover capability through which the GPSDO maintains a high-fidelity 1 PPS signal even when a GPS signal is not available, which is known to occur in deep mountainous terrain. The external clocks maintain system synchronization within tens of nanoseconds even when the stations are separated by several kilometers, are NLOS to each other, and do not have a reliable GPS signal.

Notably, system coherency allows for continuous capture durations up to 60 s. *Coherency* describes the case that the channel sounding Tx is continuously synchronized in time with the Rx, and delay time calibration (e.g., by referencing a known LOS component) during postprocessing is unnecessary. While not rigorously investigated in the present study, our analysis suggests that 1 second is sufficient time for approximating the bistatic CIR even in noisy environments. All power–delay profiles presented in the Results section of this report were generated using 5-second captures.

The power consumption of each mWISP unit is 50 W. The mWISP internal battery allows for 1.5 hours of continuous operation; and with the addition of an external, solid-state, 24 VDC, 10 A-h LiFePO₄ (lithium iron phosphate) Powerizer battery, the mWISP can operate continuously for over 6 hours. The Rb clock power consumption is approximately 20 W and with one LiFePO₄ battery is capable of operating continuously for over 8 hours. The Tx power amplifier power consumption is 85 W and with one LiFePO₄ battery is capable of operating continuously for over 2 hours. Given that the power amplifier is powered on only during transmissions, a single battery is sufficient for a full day of channel sounding. Each Getac field laptop uses two removable battery packs, collectively allowing for over 8 hours of continuous operation with a screen brightness of 70 percent. In summary, the entire system is capable of operating solely on battery power for over 6 hours with current battery resources.

Figure 1. The 23 kg station backpack: (a) from top to bottom, Getac B300 field laptop; external Rb clock; mWISP unit; two solid-state, 24 VDC, 10 A-h LiFePO₄ batteries; and GPS antenna on the right and (b) the station backpack shouldered for transport.



For the sounding measurements presented here, the Tx station used a Creative Design CLP 5130-2 log-periodic directional antenna with a 60-degree half-power beam width and a forward gain of 12 dBi. The cable between the Tx mWISP front end and the antenna attenuated the transmitted signal by roughly 2 dB. The Rx station used a Diamond Antenna D220

discone omnidirectional antenna with approximately 3 dBi of gain. The Rx cable between the station antenna and the Rx mWISP front end attenuated the received signal by roughly 1 dB. The motivation for using a directional antenna at the Tx was to pointedly deliver signal power to prominent topographic features in the environment.

2.6 Channel sounding waveform

The channel sounding waveform is a maximal length PN sequence (m-sequence) (Salous 2013). A linear feedback shift register implemented in Python (Python Core Team 2017) using the *NumPy* module (van der Walt et al. 2011) generates the 65535-bit m-sequence. The waveform is direct-sequence spread-spectrum (Rappaport 2002; Pickholtz et al. 1982; Newhall et al. 1996), binary phase-shift keying (BPSK) modulated.

The waveform is a continuously repeated PN period (i.e., -1 s and $+1$ s) with a period of silence (i.e., 0s) to synchronize the waveform with the 1 PPS edge. The number of continuous PN period repeats and the exact length of the zero padding both depend on the transmitted waveform bandwidth. Over each second, hundreds of periods of the PN sequence are transmitted and captured, each of which generates a complete power–delay-profile trace after postprocessing.

The theoretical processing gain from the cross-correlation of an m-sequence is dependent on the sequence length and the number of times each bit in the sequence is repeated (Sousa et al. 1994):

$$10 \log_{10} \left(\frac{PN \text{ Length}}{Repeat \text{ Value}} \right). \quad (8)$$

For instance, using the 65535-bit m-sequence and a repeat value of one, the theoretical maximum processing gain is approximately 48 dB.

The waveform for the channel measurements in this paper uses a 65535-bit m-sequence with a repeat value of two; thus, the m-sequence period was doubled to 131070 bits, and the effective null-to-null bandwidth of the signal was 12.5 MHz (Rappaport 2002). The range extent of this PN length is orders of magnitude greater than the ones to tens of kilometers that are relevant for ground-to-ground UHF communication systems (i.e.,

$1/(12.5\text{e6 MS/s}) \times (131070 \text{ bits}) \times (299.7\text{e6 m/s}) \approx 3100000 \text{ m} = 3100 \text{ km}$). For the channel sounding system in this paper, differences in CIR estimation with respect to measurement integration time are considered negligible after 1 second (i.e., each CIR trace completes in $1/(12.5\text{e6 MS/s}) \times (131070 \text{ bits}) = 0.0104856 \text{ s}$, thus a 1 second measurement integrates over 95 complete CIR traces).

An in-depth discussion of m-sequences, including linear feedback shift register-based generation of PN sequences and the frequency spectrum of PN sequences, can be found in Salous (2013).

2.7 System resolution and uncertainty

The maximum operational bandwidth of the system is 25 MHz (and the maximum sampling frequency is 25 MS/s), corresponding to a temporal resolution of 40 ns. This temporal resolution is a limitation of the mWISP URSP and is not exceptionally noteworthy in the channel sounding community. Many modern channel sounding systems have effective operational bandwidths that are hundreds of megahertz (Durgin et al. 2003; Ghassemzadeh et al. 2004; Li et al. 2017), providing temporal resolutions in the single nanoseconds. On the other hand, the compactness of the mWISP units enables our system to be entirely foot portable. Thus, the limited temporal resolution of the system is a tradeoff for system portability.

A waveform repeat value of two reduces the temporal resolution of the system from 40 ns (at the max sampling rate of 25 MS/s, given that BPSK modulation results in one symbol per bit) to 80 ns, but the spatial scales of the topographic features of interest far exceed the 24 m spatial resolution that corresponds to the reduced temporal resolution (i.e., $299.7 \text{ m}/\mu\text{s} \times 0.08 \mu\text{s} = 24 \text{ m}$).

Sources of system temporal uncertainty include the following:

- The transmit and capture routines programmed in each mWISP initiate on the next 1 PPS GPS edge after activation via the mWISP graphical user interface (GUI). The uncertainties associated with these routines are well-documented (mWISP Team 2016) and are functions of the transmission bandwidth and sampling rate settings

in the Tx and Rx mWISP GUIs, respectively. At a transmission bandwidth of 25 MHz and Rx sampling rate of 25 MS/s, the Tx mWISP transmit uncertainty is ± 100 ns, and the Rx mWISP capture uncertainty is ± 100 ns.

- The 1 PPS GPS signals from the two Rb clocks fire at slightly different times. We measured the 1 PPS GPS signal offset for nearly 40 hours continuously and found that the offset roughly assumed a normal distribution. We set the uncertainty contribution from the Rb clocks to be ± 30 ns (three times the standard deviation of the data set).

These uncertainties are independent; and therefore, they are summed in quadrature to determine the system-wide temporal uncertainty, which we report to be ± 145 ns (i.e., $\sqrt{(100^2 + 100^2 + 30^2)} \approx 145$ ns). This temporal uncertainty corresponds to a spatial uncertainty of ± 44 m.

2.8 Postprocessing

The Rx captures in-phase and quadrature (IQ) RF data and stores the data onboard the mWISP in binary form. Data are postprocessed using a fast cross-correlation algorithm implemented in Python (Python Core Team 2017) using the *NumPy* module (van der Walt et al. 2011). The algorithm correlates a single, zero-padded, original PN sequence period (i.e., $x[t]$) with the signal captured at the Rx (i.e., $y[t]$), yielding a series of CIR curves. With reference to equations (5)–(7), cross-correlation approximates the CIR according to

$$h[\tau] \cong F^{-1}(F(\bar{x}[t])F(y[t])). \quad (9)$$

Here, $F^{-1}(\cdot)$ is the Inverse Fast Fourier Transform; $h[\tau]$ is the CIR; $F(\bar{x}[t])$ is the Fast Fourier Transform of the complex conjugate of $x[t]$; and $F(y[t])$ is the Fast Fourier Transform of the received signal IQ data. After data handling, the result is a two-dimensional matrix of CIR traces through time. CIR data points are proportional to signal voltage with respect to time delay.

The power–delay profile, introduced in section 2.4, is normalized during postprocessing to be

$$P_{norm}[\tau] = 10 \log_{10} \langle |h[\tau]|^2 \rangle - \max(10 \log_{10} \langle |h[\tau]|^2 \rangle). \quad (10)$$

Here, the CIR quantity $h[\tau]$ is calculated from the raw IQ data and is in units of proportional to volts. Upon squaring and taking the logarithm, each term in equation (10) is in units of power proportional to dBm. However, each term in equation (10) is *not* in units of absolute power because the cross-correlation is completed in the frequency domain (equation [9]) and is not easily normalized like the definition of the time-domain cross-correlation (equation [4]). Rather, the power–delay profile, $P_{norm}[\tau]$, is normalized to the maximum received power and is presented in units of dB (i.e., the highest power profile point being 0 dB) with respect to absolute time delay. The use of normalized power is sufficient because quantitative analysis of power–delay profile time dispersion is still valid and is the priority for this study.

The captured sounding waveform gives rise to hundreds of power–delay-profile traces every second (the exact number being a function of the transmission bandwidth and corresponding Rx sampling rate). Power–delay-profile traces are averaged (in linear units of power proportional to watts) to reduce correlation noise peaks, which are assumed to be uncorrelated between measurements and uncorrelated with the desired signal. The degree of noise smoothing is related to the number of traces averaged, N . The power–delay-profile signal-to-noise ratio (SNR) improves according to $20 \log_{10}(N)$. For example, if a 25 MHz bandwidth, repeat 1 signal is captured at the Rx using a 25 MS/s sampling rate, a total of 380 power–delay-profile measurements are made and subsequently averaged, resulting in an SNR enhancement of nearly 52 dB. Note that this averaging requires the assumption that the WSSUS channel model is valid (e.g., channel statistics do not change over the duration of time averaging).

2.9 Frequency-selective fading

The delay or time spreading of a signal can lead to intersymbol interference and frequency-selective fading in the signal passband at the Rx. Intersymbol interference occurs when the same signal symbol arrives at several different times due to multipathing, leading to bit errors at the receiving station. Frequency-selective fading occurs when multipath components arrive at the receiving station near 180 degrees out of phase with one

another, causing deconstructive interference. This deconstructive interference results in steep drops in signal power at specific frequencies across the signal passband (Sklar 1997).

The occurrence of frequency-selective fading can be determined by inspecting the power–delay profile. An amplitude threshold is applied to the power–delay profile, which removes very low power noise (i.e., the “noise floor”). The resulting profile includes only data points above the threshold. (See the following section, section 2.10, for a more in-depth discussion of thresholding.) Frequency-selective fading results if the duration of the thresholded power–delay profile, τ_{Max} , exceeds the signal symbol period, T_s . In BPSK modulation, like that employed by the system here, one bit is transmitted per symbol, and the bit rate is equivalent to one-half the null-to-null transmission bandwidth, W (Rappaport 2002). Thus, the symbol period is equivalent to two times the inverse of the transmission bandwidth, $T_s = 2/W$ (Sklar 1997). For the data presented here, the transmitted signal bandwidth is 25 MHz with a repeat value of 2, which results in an effective null-to-null bandwidth of 12.5 MHz. Thus, the symbol period is 80 ns (i.e., $2/12.5e6 = 80$ ns). In summary, if the maximum excess delay exceeds the symbol period of 80 ns, frequency-selective fading is observed. Furthermore, it is irrelevant if an 80 ns interval includes power from one or multiple multipath components; if the sum of the component amplitudes does not exceed the threshold, it will not be considered for frequency-selective fading or channel statistics of any kind. Frequency-selective fading was the rule rather than the exception in our study areas, where the range extent and surface roughness scales of mountainous features ranged from tens to thousands of meters.

2.10 Channel statistics

An important channel statistic in the time domain is the root mean squared (RMS) delay spread, which is the power-weighted second central moment of the data points in the power–delay profile that lie above a correlation noise-floor threshold. The RMS delay spread is defined as (Rappaport 2002)

$$\sigma_\tau = \sqrt{\overline{\tau^2} - (\overline{\tau})^2} \quad (11)$$

where

$$\bar{\tau} = \sqrt{\frac{\sum_{i=1}^L P(\tau_i) \tau_i^2}{\sum_{i=1}^L P(\tau_i)}}. \quad (12)$$

Here, L is the total number of power–delay-profile data points, τ_i is the delay time of the i th data point, and $P(\tau_i)$ is the power of the i th data point in units of milliwatts.

A threshold separates meaningful power–delay-profile data points from the noise floor. Others in the literature set a static power–delay-profile threshold based on a need for communications analysis at 10, 20, and even 40 dB below the maximum received power, such as in Rappaport (2002), Kim et al. (2015), Joshi et al. (2005). Others investigated the influence of this threshold on channel statistics, such as in Ghassemzadeh et al. (2004).

Here, we dynamically set a threshold by

1. identifying a representative segment of noise in each power–delay profile by locating a fixed-length segment exhibiting the lowest average power in the profile,
2. calculating the average and standard deviation of this representative noise segment in units proportional to watts, and
3. setting the threshold equal to the average noise floor plus 10 times the standard deviation of the noise segment.

We created this dynamic threshold algorithm because a static threshold occasionally excluded important power–delay-profile features that matched known topographic features after geospatial analysis. Furthermore, measured power–delay profiles exhibit significantly different SNR values, from roughly 10 dB to well over 30 dB, making the selection of a reasonable static decibel threshold difficult. (While cross-correlation of the channel sounding waveform does provide substantial noise rejection, environments with high RF noise cause the profile correlation noise floor to rise substantially in some cases, e.g., in urban areas, leading to SNRs as low as 5 dB or less. We observe this phenomenon even with in-line pass-band filters upstream of the receiver USRP.)

We find that this dynamic threshold algorithm effectively separates power–delay-profile data points from the noise floor. Varela and Sanchez (2001) discuss other methods for setting the power–delay-profile noise-level threshold.

2.11 Geospatial analysis

In the mountains, the primary structures impacting the power–delay-profile shape are topographical features. Therefore, performing geospatial analyses for the various channel sounding Tx and Rx geometries can provide significant insight into the bistatic distance, and thus delay time, for a given reflecting patch of mountainside. The spatial resolution of the geospatial analysis (i.e., raster pixels ~ 8 m on a side, depending on the projection using readily available elevation datasets) is comparable to that of the effective temporal resolution of the channel sounding system discussed in section 2.7 (i.e., $299.7 \text{ m}/\mu\text{s} \times 0.08 \mu\text{s} = 24 \text{ m}$). Given the coordinates and elevations of the Tx and Rx, relatively straightforward geospatial processing generates a number of useful products from a study area digital elevation model (DEM):

- Separate viewsheds for Tx and Rx. A viewshed is the region of a DEM that is (optically) visible from the point of interest.
- Covisible regions for the Tx and Rx pair (i.e., both the Tx and Rx have LOS to the regions in question). The Tx and Rx viewsheds are combined through an *and* operation to yield the regions directly viewable from both locations. For UHF signals, the covisible regions are a reasonable approximation of the primary reflecting surfaces in the NLOS channel. The magnitude of the reflected power from a given patch should be approximately proportional to its area, making the simplifying assumption of constant reflectivity and ignoring the effects of slope and aspect on scattering.
- Three-dimensional (3-D), bistatic distance from the Tx to a covisible DEM point to the Rx (assuming a reflected path). From this data, contours of constant delay time are created, allowing the prediction of the arrival times of a reflection from a given covisible patch of mountainside.

Geospatial analysis is needed to identify the locations of important topographic reflectors within the measurement area because the Rx antenna was omnidirectional (which is consistent with typical and practical antennas used in the field). The assumption is made that, in general, primary reflected paths between Tx and Rx stations are the most important, and multi-reflected components are of less importance. The proper operation of the channel sounding system is verified by matching peaks in the power–delay profile with topographic features that share the same bistatic delay times.

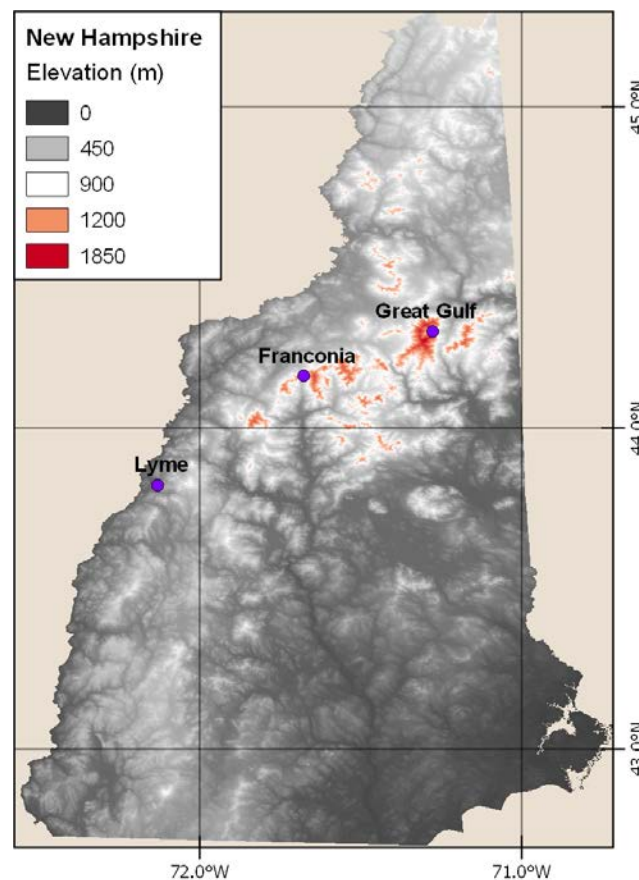
Open-source geographic information system (GIS) software, QGIS (QGIS Development Team 2017), performed the geospatial analyses, supplemented by Python (Python Core Team 2017) scripting. DEMs were derived from the 1/3 arc-second elevation database accessed via the U.S. National Map (Dollison 2010). The elevation data were projected into the appropriate Universal Transverse Mercator coordinate systems (i.e., 19N for Great Gulf and Franconia Notch studies areas; 18N for the Lyme area) to allow straightforward calculation of distances between points within the DEM. Earth curvature was ignored in the viewshed calculations, as the typical ranges to covisible reflectors are 15 km or less. Viewshed analyses and contouring within QGIS were performed with the *r.viewshed* and *r.contour.step* modules of the Geographic Resources Analysis Support System (commonly known as GRASS) (Haverkort et al. 2009; GRASS Development Team 2017; Neteler et al. 2012). The *Rasterio* Python module (Gillies et al. 2013) enabled the calculation of bistatic distances and delay times as a function of geographic location.

The resulting bistatic delay time contours were overlaid directly on the DEM and covisible area GIS layers, enabling both verification of proper channel sounding system timing and insight into the intimate relationship between the geometry of mountainous regions and the RF channels that the mountains create.

3 Channel Measurement Results

We performed channel sounding measurements in three mountainous study areas in New Hampshire to test the system in several different geographies. The tests, conducted at a center frequency of 437 MHz for only bi-static Tx–Rx configurations, verify proper correspondence of the power–delay profiles with various topographic reflectors identified by geospatial analysis. Figure 2 shows the study areas, which generally lie within the northeast–southwest belt of mountainous terrain running across the state. We present these areas in order of increasing topographic and channel complexity: Franconia Notch, Great Gulf Wilderness, and finally Lyme, the last of which counterintuitively features both the lowest topographic relief and the most complex channel characteristics.

Figure 2. The state of New Hampshire and the three-channel sounding study areas.



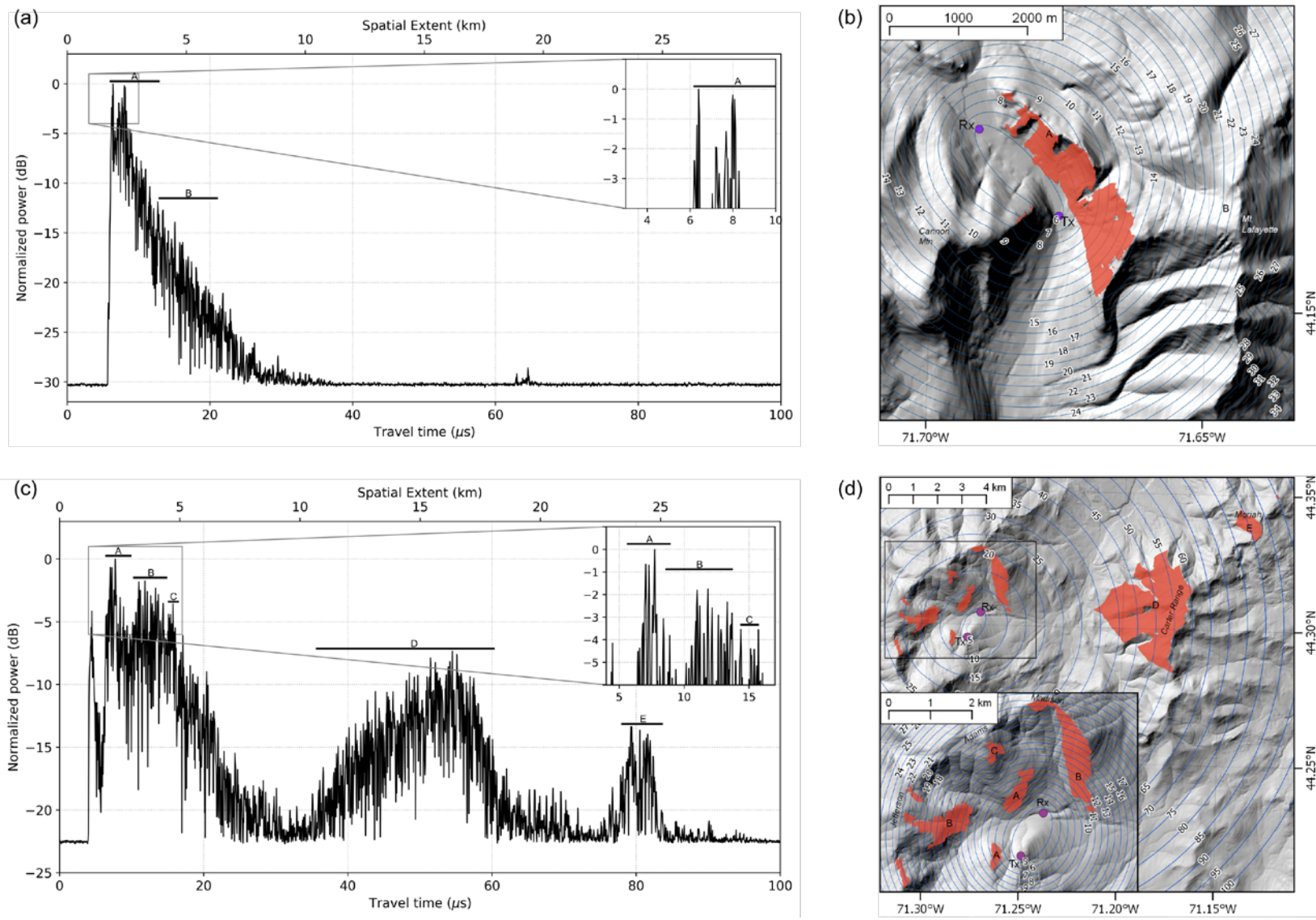
We present four example power–delay profiles from the three study areas: one from Franconia Notch, one from the Great Gulf Wilderness, and two from Lyme. Frequency-selective fading is observed in every power–delay profile presented as the maximum excess delay time, τ_{Max} , introduced in section 2.9, which far exceeds the symbol period of 80 ns. The power–delay profiles have very different noise-floor power levels, a consequence of having a wideband SDR *without* analog preselection filtering on the Rx front end (Papazian and Lemmon 2011). For measurements in particularly remote locations, the RF noise was minimal. However, in closer proximity to cell towers, repeaters, and populated areas, the Rx suffered more RF noise.

3.1 Franconia Notch study area

Franconia Notch is a narrow, postglacial valley that creates a NLOS channel around the prominent base of Cannon Mountain immediately to the west of the Tx location, as shown in Figure 3b. The valley floor is approximately 500 m below the surrounding mountain ridges. The valley floor and the slopes up to the ridgelines are covered in dense, coniferous forest with patches of exposed bedrock. A LOS path between the Tx and Rx would require 5.7 μs of travel time. Geospatial analysis of this area shows a covisible patch, labeled A in in Figure 3b, along the eastern wall of the Notch with predicted reflection arrival times of 6–13 μs . Beyond this, no single scattered paths exist between the Tx and Rx, thus we have a simple NLOS channel formed by a single, geospatially contiguous reflector.

Figure 3a shows the power–delay profile measured in Franconia Notch, indicating a weak arrival at 5.8 μs (likely diffraction around the base of Cannon Mountain) followed by a rapid rise in power, peaking at 6.4 and 8.1 μs . Beyond 8 μs , we have a significant reduction in covisible area; and past 13 μs , the covisible area drops to zero. The power–delay profile takes on at least two distinct slopes: $-2.8 \text{ dB}/\mu\text{s}$ on 8–13 μs and $-1.1 \text{ dB}/\mu\text{s}$ on 13–23 μs , suggesting that the channel is influenced by regions beyond the covisible ones. The 13–23 μs bistatic delay time segment encompasses the west-facing slopes of Mt. Lafayette and the Franconia Range (labeled region B along the eastern side of Figure 3b), which are likely the cause of the received signal during this time period.

Figure 3. Sounding results (5 s capture time for each profile) coupled with geospatial analysis. Covisible regions are highlighted in *red*, and *concentric blue rings* show bistatic path delay time on the maps: (a) power-delay profile from Franconia Notch, (b) map of the Franconia Notch area, (c) power-delay profile from the Great Gulf Wilderness, and (d) map of the Great Gulf Wilderness area.



3.2 Great Gulf Wilderness study area

The Great Gulf Wilderness is a large, postglacial valley surrounded by the tallest peaks in the White Mountains with approximately 1000 m of relief, as shown in Figure 3d. The terrain is covered by dense, coniferous forest, giving way to scree fields and exposed bedrock at higher elevations. The study area is surrounded by the Presidential Range to the north and west, and the Carter Range lies about 10 km to the east. This map shows a complex geospatial scenario with many separate covisible patches, some of which overlap in bistatic delay time.

The corresponding Great Gulf Wilderness power–delay profile is shown in Figure 3c, showing three distinct clusters of power from separate topographic reflectors. The Tx–Rx pair was separated by 1.16 km horizontally and 453 m of elevation with no LOS existing between the stations. The first cluster is associated with reflections from within the confines of the Great Gulf itself, which has covisible areas with bistatic delays from 6 to 23 μ s. The second cluster, from 37 to 60 μ s, is composed of reflections from the Carter Range; and the final cluster, around 80 μ s, is a reflection from Mt. Moriah, some 14 km to the northeast of the Tx–Rx pair.

While many of the covisible patches overlap in delay time within these clusters, individual propagation paths and reflectors can be still be identified, as shown in the inset of Figure 3c. The earliest arriving component at 4.5 μ s is most likely diffracted downslope from the Tx to the Rx, as the direct LOS path delay is predicted to be 4.15 μ s based on the 3-D separation distance of 1.25 km. Reflections from the patches labeled A arrive at 7.5 μ s, followed by the two large areas labeled B, which reflect signals from 11 to 17 μ s. The reflecting patch labeled C just below the summit of Mt. Adams appears at 16 μ s and is the last distinct reflector we observe within the Great Gulf proper.

The more distant reflections from the Carter Range and Mt. Moriah have geospatially plausible first arrival times and reflection durations of 25 and 7 μ s, respectively, consistent with the spatial extent of the covisible areas D and E shown in Figure 3d.

3.3 Lyme study area

The Ranger Trail and Acorn Hill Road areas are within the town of Lyme, New Hampshire. The terrain is mainly dense, mixed forest covering rolling hills and deep ravines with patches of open fields in low areas. The hills provide 300–600 m of relief and are mostly tree covered, including the summit of Smarts Mountain, the highest point in the study area at an elevation of 985 m. We show two examples from this area: a measurement made on foot on the Ranger Trail and a roadside measurement on Acorn Hill.

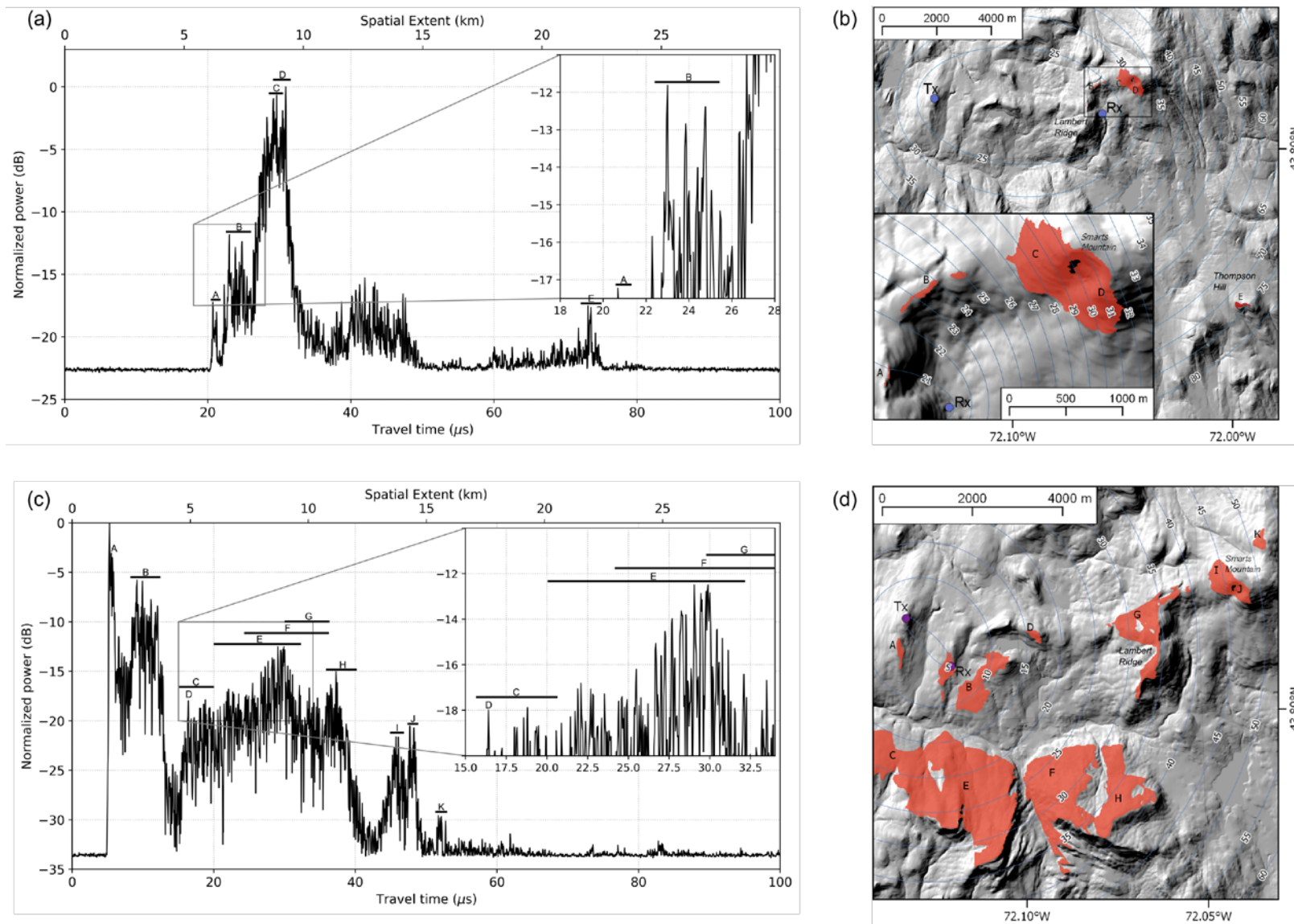
3.3.1 Ranger Trail

This geometry involves a severely NLOS Tx–Rx configuration with the Rx along the Ranger Trail; Figure 4a and b show the power–delay profile and bistatic delay map, respectively. In this geometry, the first arrival at 20.8 μs is very close to the minimum possible delay time of 20.7 μs based on a 6.20 km direct 3-D Tx–Rx separation, suggesting that signal components reach the Rx via the small covisible area labeled A or possibly diffract directly over Lambert Ridge. The covisible patch B on the same ridge-line covers the 22.5–25 μs period and has three distinct reflectors visible in the power–delay profile. The strongest propagation paths occur in two separate arrivals at 29.4 and 30.6 μs , corresponding to patches C and D, respectively, both near the summit of Smarts Mountain. The covisibility analysis *does not* predict the 40–49 μs arrival shown in the power–delay profile, suggesting that diffraction and subsequent reflection may be the responsible type of propagation path during this time period. The last return at 73.5 μs is from the covisible patch on Thompson Hill, labeled E in Figure 4b, approximately 13.6 km from the Tx.

3.3.1 Acorn Hill

This geometry includes both LOS and multiple overlapping reflection arrivals as seen in Figure 4c. Figure 4d shows the bistatic delay map for this geometry and the large covisible areas, which overlap in delay time. These overlaps and the number of separate covisible patches give rise to our most complex channel.

Figure 4. Sounding results (5 s capture time for each profile) coupled with geospatial analysis. Covisible regions are highlighted in *red*, and *concentric blue rings* show bistatic path delay time on the GIS maps: (a) power-delay profile from Ranger Trail in Lyme, (b) map of the Ranger Trail area, (c) power-delay profile from Acorn Hill in Lyme, and (d) map of the Acorn Hill area.

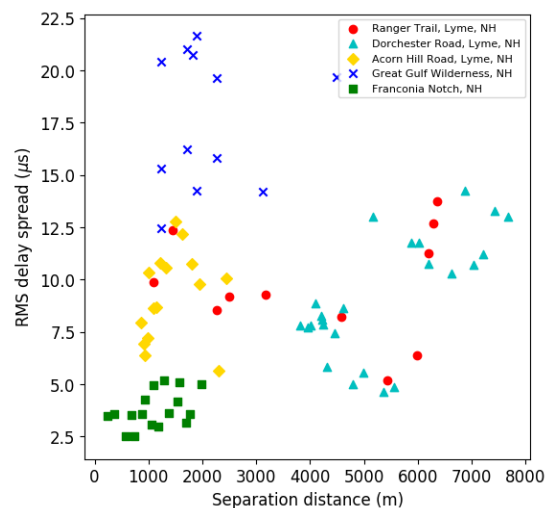


The covisibility analysis indicates that the Tx and Rx have LOS in this geometry; and we observe the first arrival at 5.0 μs , compared to the minimum possible delay time of 4.85 μs based on the 1.45 km Tx–Rx separation. The 0.15 μs disagreement in arrival time is consistent with the overall timing uncertainty of the system. Covisible patch B is observed in the power–delay profile from 8 to 12 μs , followed by multiple overlapping arrivals from patches C through H, corresponding to delay times of 15–39 μs . Patches I, J and K, all located in the vicinity of the Smarts Mountain summit, are clearly separated in the power–delay profile and match the geospatially predicted arrival times within the timing uncertainty of the sounding system.

3.4 Channel statistics

The four power–delay profiles presented here are quite different in character but all arise from channels in mountainous terrain. We plotted the RMS delay spread (equation [11]) with respect to 3-D Tx–Rx separation distance for 79 total measurements in the three study areas, as shown in Figure 5, for a broad comparison of channel character between the three study areas. (Lyme data are broken into three subsets, as shown in the legend.)

Figure 5. RMS delay spread data presented as a function of 3-D Tx–Rx separation distance for the three main study areas. A total of 79 profile RMS delay spreads are reported.



The clustering effects observed in Figure 5 suggest that different locations generate a wide variety of time dispersion behaviors in the channel depending on the terrain and the geometry of the communicating stations. Channel statistics may be drastically different between mountainous areas, whether communications occur adjacent to or within the mountains and whether communicating stations are at similar elevations. Additionally, these variations may be related to geomorphometric concepts that can quantitatively describe the shape and spatial frequency of land surface structures (Pike 1988, 2000).

4 Discussion

For both simple (e.g., Franconia) and complex (e.g., Lyme) channels, we find good agreement between the measured power–delay profiles and the corresponding geospatial analyses. Major reflectors are observed within about 150 ns of the geospatially predicted bistatic delay time, consistent with the known timing uncertainties of the sounding system. Diffraction effects, not currently included in the geospatial analysis workflow, do appear to impact the channel in measureable ways and were observed in all four of the examples shown here. Important multipath components in NLOS channels appear to be dominated by primary reflection but also may include paths that involve multiple diffraction and/or reflection instances.

Beyond simple verification of the sounding system, this dataset gives insight into the wide variety of RF channels existing in mountainous terrain and their intimate relationship to the shared geometry of the Tx, Rx, and environment. Geospatial analysis appears to be a useful method of channel characterization in mountainous terrain where large spatial scales and rough reflecting surfaces (i.e., sub- λ to tens of meters in scale) make computational approaches burdensome. Ray-tracing models might provide a valuable comparison to the experimental work presented herein (Vitucci et al. 2015). However, we note that ray tracing generally applies to geometries with dimensions that are much greater than the signal wavelength; and thus, surface roughness effects would likely be lost by ray-tracing analysis.

5 Conclusion

In this report, we introduce a portable, spread-spectrum, SDR-based channel sounding system and validate the system using geospatial analysis. The system maintains a temporal uncertainty of ± 145 ns (spatial uncertainty of ± 44 m) and exhibits 30-plus dB of dynamic range. Power–delay profiles characterizing the UHF channel in three study areas demonstrate the intimate relationship that exists between the shared geometry of the Tx, the Rx, and the surrounding topography.

RMS delay spread measurements from the three study areas exhibit obvious clustering effects, suggesting that channel statistics in one mountainous area will not necessarily be applicable in other areas. Thus, channel statistics may be an inadequate method of general channel characterization for RF propagation and communication planning tools in mountainous terrain.

A greater understanding of how local topography influences RF propagation may improve propagation planning tools. Such improvements would empower field-deployed ground stations, such as military forces in denied territory or rescue personnel in the backcountry, with improved UHF communications decision making. Specifically, we hypothesize that the exploitation of specific topographic features as purposeful RF signal reflectors may improve ground communications in mountainous terrain. This hypothesis is supported by the measurements presented here and motivates future work on RF propagation in the mountains.

6 Future Work

We made improvements to the channel sounding system in preparation for the 2017 field season. Coaxial bandpass filters now provide analog pre-selection filtering, thereby reducing interference suffered at the Rx. The Tx station is backpack-mounted like the Rx station, so the entire system is fully mobile. Both stations have identical power amplifiers, thereby enabling full-functioning, two-way channel sounding in mountainous terrain. During the 2017 field season, we successfully collected two-way channel sounding measurements in the Lyme and Great Gulf Wilderness study areas. We hope to use these data to test the validity of assumptions regarding channel reciprocity in mountainous channels.

The data and analysis presented in this report do not exploit the long capture times that the system is capable of measuring (i.e., up to 60 seconds continuously). Future work could investigate the transience of total signal power through time and the power and phase within specific bins of the power–delay profile through time. Resulting measurements could then be compared to theoretical fading distributions to show a unique snapshot of channel transience and quality in the mountains.

We aim to deterministically estimate power–delay profiles for NLOS channels in mountainous terrain by augmenting our geospatial analysis. Incorporating mountain slope, aspect, antenna patterns, and reflectivity information could form the basis for this type of estimation, like that discussed in Driessen (2000) and Xiao et al. (2010). Theoretical power–delay profiles for complex Tx, Rx, and environment geometries could then be validated using our portable channel sounding system. The creation of such a model is currently in progress. Furthermore, useful comparisons could be made with existing theoretical models, like Remcom’s Wireless InSight X3D ray-tracing model (Remcom 2016).

References

- Breton, D. J., and S. A. Arcone. 2015. Radiofrequency Speckle in Mountainous Terrain. In *Proceedings, 2015 IEEE International Symposium on Antennas and Propagation USNC/URSI National Radio Science Meeting*, 19–24 July, Vancouver, BC, Canada, 997–998.
- Bultitude, R. 1987. Measured Characteristics of 800/900 MHz Fading Radio Channels with High Angle Propagation Through Moderately Dense Foliage. *IEEE Journal on Selected Areas in Communications* 5 (2): 116–127.
- Chuang, J. 1987. The Effects of Time Delay Spread on Portable Radio Communications Channels with Digital Modulation. *IEEE Journal on Selected Areas in Communications* 5 (5): 879–889.
- Cox, D., and R. Leck. 1975. Correlation Bandwidth and Delay Spread Multipath Propagation Statistics for 910-MHz Urban Mobile Radio Channels. *IEEE Transactions on Communications* 23 (11): 1271–1280.
- de Weck, J. P., P. Merki, and R. W. Lorenz. 1988. Power Delay Profiles Measured in Mountainous Terrain. In *Proceedings, 38th IEEE Vehicular Technology Conference*, 15–17 June, Philadelphia, PA, 105–112.
- Dollison, R. M. 2010. *The National Map: New Viewer, Services, and Data Download*. U.S. Geological Survey Fact Sheet 2010–3055. <https://pubs.usgs.gov/fs/2010/3055/>.
- Doukas, A., and G. Kalivas. 2006. Rician K Factor Estimation for Wireless Communication Systems. In *Proceedings, 2006 International Conference on Wireless and Mobile Communications (ICWMC'06)*, 29–31 July, Bucharest, Romania, 117–123.
- Driessen, P. F. 1990. Measured Propagation Characteristics of 900 MHz Mobile Radio Channels in Mountainous Terrain. In *Proceedings, 40th IEEE Conference on Vehicular Technology*, 6–9 May, Orlando, FL, 603–609.
- . 1991. Multipath Delay Characteristics in Mountainous Terrain-Comparison of Theoretical Predictions with Measurement Results. In *Proceedings, 41st IEEE Vehicular Technology Conference*, 19–22 May, St. Louis, MO, 606–609.
- . 1992. Multipath Delay Characteristics in Mountainous Terrain at 900 MHz. In *Proceedings, Vehicular Technology Society 42nd VTS Conference—Frontiers of Technology*, 10–13 May, Denver, CO, 1:520–523.
- . 2000. Prediction of Multipath Delay Profiles in Mountainous Terrain. *IEEE Journal on Selected Areas in Communications* 18 (3): 336–346.
- Durgin, G. D., V. Kukshya, and T. S. Rappaport. 2003. Wideband Measurements of Angle and Delay Dispersion for Outdoor and Indoor Peer-to-Peer Radio Channels at 1920 MHz. *IEEE Transactions on Antennas and Propagation* 51 (5): 936–944.
- Gans, M. J. 1972. A Power-Spectral Theory of Propagation in the Mobile-Radio Environment. *IEEE Transactions on Vehicular Technology* 21 (1): 27–38.

- Ghassemzadeh, S. S., R. Jana, C. W. Rice, W. Turin, and V. Tarokh. 2004. Measurement and Modeling of an Ultra-Wide Bandwidth Indoor Channel. *IEEE Transactions on Communications* 52 (10): 1786–1796.
- Gillies, S., et al. 2013. Rasterio: Geospatial Raster I/O for Python Programmers. Mapbox, 2013–. <https://github.com/mapbox/rasterio>.
- GRASS Development Team. 2017. Geographic Resources Analysis Support System (GRASS GIS) Software, Version 7.2. Open Source Geospatial Foundation. <http://grass.osgeo.org>.
- Haverkort, H., L. Toma, and Y. Zhuang. 2009. Computing Visibility on Terrains in External Memory. *Journal of Experimental Algorithmics (JEA)* 13:1.5.
- Joshi, G. G., C. B. Dietrich, C. R. Anderson, W. G. Newhall, W. A. Davis, J. Isaacs, and G. Barnett. 2005. Near-Ground Channel Measurements over Line-of-Sight and Forested Paths. In *IEEE Proceedings, Microwaves, Antennas and Propagation* 152 (6): 589–596.
- Kim, M. D., J. Lee, J. Liang, and J. Kim. 2015. Multipath Channel Characteristics for Propagation between Mobile Terminals in Urban Street Canyon Environments. In *Proceedings, 2015 17th International Conference on Advanced Communication Technology (ICACT)*, 1–3 July, Seoul, South Korea, 511–516.
- Li, J., Y. Zhao, C. Tao, and B. Ai. 2017. System Design and Calibration for Wideband Channel Sounding With Multiple Frequency Bands. *IEEE Access* 5:781–793.
- Lu, J. S., and H. L. Bertoni. 2013. A Site-Specific MIMO Channel Simulator for Hilly and Mountainous Environments. In *Proceedings, MILCOM 2013–2013 IEEE Military Communications Conference*, 18–20 November, San Diego, CA, 764–769.
- Lu, J. S., X. Han, and H. L. Bertoni. 2013. The Influence of Terrain Scattering on Radio Links in Hilly/Mountainous Regions. *IEEE Transactions on Antennas and Propagation* 61 (3): 1385–1395.
- Maeyama, T., F. Ikegami, and Y. Kitano. 1993. Analysis of Mountain-Reflected Signal Strength in Digital Mobile Radio Communications. *IEICE Transactions on Communications* 76 (2): 98–102.
- Mohr, W. 1993. Wideband Propagation Measurements of Mobile Radio Channels in Mountainous Areas in the 1800 MHz Frequency Range. In *Proceedings, IEEE 43rd Vehicular Technology Conference*, 18–20 May, Secaucus, NJ, 49–52.
- mWISP Team. 2015. *mWISP Help Pages*. Rev. 7.0.2015.4 ed. Sterling, VA: Echo Ridge LCC.
- Neteler, M., M. H. Bowman, M. Landa, and M. Metz. 2012. GRASS GIS: A Multi-Purpose Open Source GIS. *Environmental Modelling and Software* 31:124–130.
- Newhall, W. G., T. Rappaport, and D. G. Sweeney. 1996. A Spread Spectrum Sliding Correlator System for Propagation Measurements. *RF Design Magazine*, 40–54.

- Novosel, L., and G. Šišul. 2014. Comparison of Pseudo Noise Sequence Lengths for a Correlator Channel Sounder. In *Proceedings, 56th International Symposium ELMAR-2014*, 10–12 September, Zadar, Croatia, 139–142.
- Papazian, P., and J. Lemmon. 2011. *Radio Channel Impulse Response Measurement and Analysis*. NTIA Technical Report TR-11-476. Washington, DC: U.S. Department of Commerce, National Telecommunications & Information Administration.
- Pickholtz, R., D. Schilling, and L. Milstein. 1982. Theory of Spread-Spectrum Communications—A Tutorial. *IEEE Transactions on Communications* 30 (5): 855–884.
- Pike, R. J. 1988. The Geometric Signature: Quantifying Landslide-Terrain Types from Digital Elevation Models. *Mathematical Geology* 20 (5): 491–511.
- . 2000. Geomorphometry-Diversity in Quantitative Surface Analysis. *Progress in Physical Geography* 24 (1): 1–20.
- Python Core Team. 2017. Python 3.6.4. Python Software Foundation. <https://www.python.org/downloads/release/python-364/>.
- QGIS Development Team. 2017. QGIS Geographic Information System, Open Source Geospatial Foundation. <https://www.qgis.org/en/site/>.
- Raekken, R. H., H. Langaas, G. Lovnes, and S. E. Paulsen. 1991. Wideband Impulse Response Measurements at 900 MHz and 1.7 GHz. In *Proceedings, Global Telecommunications Conference, 1991. GLOBECOM '91. Countdown to the New Millennium. Featuring a Mini-Theme on: Personal Communications Services*, 2–5 December, Phoenix, AZ, 2:1303–1307.
- Rappaport, T. S. 2002. *Wireless Communications: Principles and Practice*. 2nd ed. Upper Saddle River, NJ: Prentice Hall PTR.
- Remcom. 2016. *Wireless InSite Reference Manual Version 2.8.1*. State College, PA: Remcom.
- Salous, S. 2013. *Radio Propagation Measurement and Channel Modelling*. Chichester, UK: John Wiley and Sons Ltd.
- Sklar, B. 1997. Rayleigh Fading Channels in Mobile Digital Communication Systems. Part I. Characterization. *IEEE Communications Magazine* 35 (9): 136–146.
- Sousa, E. S., V. M. Jovanovic, and C. Daigneault. 1994. Delay Spread Measurements for the Digital Cellular Channel in Toronto. *IEEE Transactions on Vehicular Technology* 43 (4): 837–847.
- van der Walt, S., S. C. Colbert, and G. Varoquaux. 2011. The NumPy Array: A Structure for Efficient Numerical Computation. *Computing in Science Engineering* 13 (2): 22–30.
- Varela, M. S., and M. G. Sanchez. 2001. RMS Delay and Coherence Bandwidth Measurements in Indoor Radio Channels in the UHF band. *IEEE Transactions on Vehicular Technology* 50 (2): 515–525.

- Vitucci, E., V. Degli-Esposti, F. Fuschini, J. Lu, M. Barbiroli, J. Wu, M. Zoli, J. Zhu, and H. Bertoni. 2015. Ray Tracing RF Field Prediction: An Unforgiving Validation. *International Journal of Antennas and Propagation* 2015:184608.
- Xiao, A. H., H. L. Bertoni, C. Chrysanthou, and J. Boksiner. 2010. Fast Prediction of Scattering in Mountainous Terrain Using Commonly Visible Surfaces. In *Proceedings, 2010 IEEE Sarnoff Symposium*, 12–14 April, Princeton, NJ, 1–5.
- Zogg, A. 1987. Multipath Delay Spread in a Hilly Region at 210 MHz. *IEEE Transactions on Vehicular Technology* 36 (4), 184–187.

REPORT DOCUMENTATION PAGE

Form Approved
OMB No. 0704-0188

Public reporting burden for this collection of information is estimated to average 1 hour per response, including the time for reviewing instructions, searching existing data sources, gathering and maintaining the data needed, and completing and reviewing this collection of information. Send comments regarding this burden estimate or any other aspect of this collection of information, including suggestions for reducing this burden to Department of Defense, Washington Headquarters Services, Directorate for Information Operations and Reports (0704-0188), 1215 Jefferson Davis Highway, Suite 1204, Arlington, VA 22202-4302. Respondents should be aware that notwithstanding any other provision of law, no person shall be subject to any penalty for failing to comply with a collection of information if it does not display a currently valid OMB control number. **PLEASE DO NOT RETURN YOUR FORM TO THE ABOVE ADDRESS.**

1. REPORT DATE (DD-MM-YYYY) March 2018			2. REPORT TYPE Technical Report/Final		3. DATES COVERED (From - To)	
4. TITLE AND SUBTITLE Measuring the Non-Line-of-Sight Ultra-High-Frequency Channel in Mountainous Terrain: A Spread Spectrum, Portable Channel Sounder					5a. CONTRACT NUMBER	
					5b. GRANT NUMBER	
					5c. PROGRAM ELEMENT NUMBER	
6. AUTHOR(S) Samuel S. Streeter, Daniel J. Breton, and Johnathan M. Corgan					5d. PROJECT NUMBER 462178	
					5e. TASK NUMBER	
					5f. WORK UNIT NUMBER	
7. PERFORMING ORGANIZATION NAME(S) AND ADDRESS(ES) U.S. Army Engineer Research and Development Center (ERDC) Cold Regions Research and Engineering Laboratory (CRREL) 72 Lyme Road Hanover, NH 03755-1290					8. PERFORMING ORGANIZATION REPORT NUMBER ERDC/CRREL TR-18-3	
9. SPONSORING / MONITORING AGENCY NAME(S) AND ADDRESS(ES) U.S. Army Corps of Engineers Washington, DC 20314-1000					10. SPONSOR/MONITOR'S ACRONYM(S) USACE	
					11. SPONSOR/MONITOR'S REPORT NUMBER(S)	
12. DISTRIBUTION / AVAILABILITY STATEMENT Approved for public release; distribution is unlimited.						
13. SUPPLEMENTARY NOTES ERDC 6.1 Basic Research						
14. ABSTRACT Very few measurements campaigns have conducted ground-based, radio-frequency propagation field measurement campaigns conducted in deep mountainous terrain, and none have focused on the non-line-of-sight channel in mountain shadow zones. Here, we introduce a versatile, spread-spectrum, portable channel sounder specifically designed to measure the non-line-of-sight, ultra-high-frequency channel in mountainous terrain. The receiver is backpack mounted for ease of transport into remote, mountainous locations that are kilometers from the transmitter and inaccessible to vehicles of any kind. The system uses software-defined radios to transmit and capture a wideband pseudorandom noise waveform and maintains synchronization using reference signals from rubidium clocks trained by global positioning system signals. A clock holdover capability maintains system synchronization within tens of nanoseconds even when global positioning system signals are unavailable. System synchronization allows for coherent captures up to 60 seconds in duration and provides a dynamic range of more than 30 decibels. The system exhibits a timing uncertainty of ± 145 nanoseconds, corresponding to ± 44 meters. Measured channel power-delay profiles are verified using geospatial analyses. Initial results suggest that local topography strongly affects channel time dispersion characteristics and that a given set of channel conditions cannot be readily generalized to cover an entire mountainous region.						
15. SUBJECT TERMS Fading channels (Radio), Mountains--New Hampshire, Radio wave propagation--Measurements, Signal processing, Software radio						
16. SECURITY CLASSIFICATION OF:				17. LIMITATION OF ABSTRACT	18. NUMBER OF PAGES	19a. NAME OF RESPONSIBLE PERSON
a. REPORT Unclassified	b. ABSTRACT Unclassified	c. THIS PAGE Unclassified	19b. TELEPHONE NUMBER (include area code)			